Applied Catalysis B: Environmental 88 (2009) 305–314

Contents lists available at ScienceDirect

Applied Catalysis B: Environmental

journal homepage: www.elsevier.com/locate/apcatb

Effects of iron and cerium in $La_{1-y}Ce_yCo_{1-x}Fe_xO_3$ perovskites as catalysts for VOC oxidation

B. Levasseur, S. Kaliaguine *

Department of Chemical Engineering, Laval University, Sainte-Foy, Qc, Canada G1K 7P4

ARTICLE INFO

Article history:
Received 7 July 2008
Received in revised form 6 November 2008
Accepted 7 November 2008
Available online 14 November 2008

Keywords:
Perovskite
Iron
Cerium
VOC oxidation
Thermodesorption experiments
Electronegativity
Carbonates

ABSTRACT

Perovskite-type mixed oxides $La_{1-y}Ce_yCo_{1-x}Fe_xO_3$ with high specific surface area were prepared by reactive grinding. These catalysts were characterized by N_2 adsorption, X-ray diffraction, oxygen storage capacity (OSC), H_2-temperature-programmed reduction (TPR-H_2), O_2-, and CH_3OH-temperature-programmed desorption (TPD). The catalytic performance of the samples for volatile organic compounds (VOC), CH_3OH, CO and CH_4 oxidation was evaluated. Cerium allows an enhancement of the reducibility of the B-site cations in perovskite structure during OSC and TPR-H_2 and an increase in the amount of β-O_2 desorbed during TPD-O_2. As opposed to cerium, the addition of iron in the perovskite structure causes a drop in B-site cations reducibility and a decrease of the oxygen mobility in the bulk. As a consequence, the catalytic activity in VOC oxidation is enhanced by introduction of cerium and weakened by iron in the lattice.

© 2008 Elsevier B.V. All rights reserved.

1. Introduction

Perovskite-type mixed oxides have been widely studied for the last four decades. These materials present an ABO_3 formula, with the tolerance factor defined by Goldschmidt [1] as: $t = (r_A + r_O)/\sqrt{2}(r_B + r_O)$, where r_A, r_B and r_O are the ionic radii for the ions A, B and O. Perovskite structures are obtained at $0.8 < t < 1$. Their high catalytic activity was reported for a wide set of reactions and particularly for oxidation reactions of hydrocarbons and volatile organic compounds. Cobalt- and manganese-based perovskites were usually reported as the two most efficient structures in oxidation reactions and they were even proposed as an alternative to noble metal supported catalysts since they present similar activities in oxidation and a lower synthesis cost [2–7]. However the low specific surface area generally displayed by these solids is still the major impediment to their use. In spite of the numerous synthesis procedures developed including: coprecipitation [8], citrate complexation [9], spray drying [4], freeze drying [10] and flame hydrolysis [11] the specific surface area observed rarely exceeds 25 m^2/g. The calcination required for crystallization has been usually pointed out as responsible for this situation since the decrease in specific surface area occurs according to a sintering process. Reactive grinding allows the synthesis of mixed oxides including perovskites at rather low temperature owing to the replacement of the thermal treatment by a mechanical treatment [12]. The nanometric structure and the high specific surface area (over 100 m^2/g) displayed by these oxides when prepared by reactive grinding have been reported [13]. The Québec firm Nanox Inc. has installed a demonstration unit of reactive grinding for the production of perovskites with capacity of 15 t/y.

As a result of our previous studies, the iron contamination induced by the use of stainless steel balls during the grinding process has been underlined [14]. Royer et al. [14] indeed indicated that some iron traces in the perovskite structure lead to a decrease of its intrinsic activity in methane oxidation. They also evaluated the impact of this iron content in isotopic exchange experiments and they were able to relate the presence of iron in perovskite and the low mobility of oxygen in the bulk of the structure [15]. This indicates that the reoxidation of the active sites during the methane oxidation may be limited by oxygen mobility in the perovskite lattice since this oxidation reaction occurs according to a Mars–Van-Krevelen mechanism.

Cerium is usually reported as a good promoter in perovskite lattice. According to several studies, partial substitution of 10% of La by Ce in cobalt or manganese-based perovskites leads to an increase in catalytic oxidation activity including propane [16], CO [17], CH_4 [18] and ethanol [19]. Reducibility and oxygen desorption, were also found to be enhanced when cerium was added in the perovskite lattice [16,20]. However, over 10% cerium in the structure causes some segregation: phases of CeO_2 appear which provokes a decrease in catalytic activity.

* Corresponding author. Tel.: +1 418 656 2708; fax: +1 418 656 3810.
E-mail address: serge.kaliaguine@gch.ulaval.ca (S. Kaliaguine).

0926-3373/$ – see front matter © 2008 Elsevier B.V. All rights reserved.
doi:10.1016/j.apcatb.2008.11.007

This paper deals with the effect of partial substitution of cerium and iron on the catalytic activity in VOC oxidation. In this study, five cobalt-based perovskite-type oxides were prepared with different cerium and iron contents. These solids were characterized by X-ray diffraction, temperature-programmed reduction by hydrogen (TPR-H_2) and temperature-programmed desorption of oxygen (TPD-O_2) and methanol (TPD-CH_3OH). Their activity was also evaluated in three different oxidation reactions (CH_3OH, CO and CH_4). The aim of this work is to understand the promotor effect usually associated to the cerium in literature and the inhibitory effect induced by the presence of iron in the perovskite structure.

2. Experimental

2.1. Catalysts preparation

Five samples of perovskites-type materials were prepared, by reactive grinding ($LaCoO_3$, $LaCo_{0.8}Fe_{0.2}O_3$, $LaCo_{0.6}Fe_{0.4}O_3$, $LaFeO_3$ and $La_{0.9}Ce_{0.1}CoO_3$). They were synthesised by grinding the single oxides. The precursors were first calcined at 600 °C and then introduced in a SPEX laboratory grinder for a first grinding during 4 h under O_2. After this step the perovskite phase was obtained but a second grinding was performed in order to increase the specific surface area [13]. NaCl or ZnO was then introduced as an additive in a weight ratio perovskite/additive = 1. Then the obtained powder was repeatedly washed with diluted NH_4NO_3 (if the additive was ZnO) or with water (if the additive was NaCl) in both cases in order to leach the additive from the sample. Finally the perovskite was calcined under air at 550 °C for 6 h.

2.2. Catalysts characterization

Surface specific areas were obtained from adsorption/desorption isotherms of N_2 at −196 °C determined using an OMNISORB apparatus. Before adsorption the samples were first evacuated for 6 h at 200 °C to remove moisture. The specific surface area was then determined from the linear part of the BET curve. The crystalline phases identification was done by X-ray diffraction using a SIEMENS D5000 diffractometer and Cu Kα radiation (λ = 1.5406 Å). Diffractograms were recorded with a step of 0.05° for 2θ between 15° and 75°. Phase recognition was made by comparison with JCPDS files. Particle sizes (D) were evaluated by means of the Scherrer equation $D = K\lambda/(\beta\cos\theta)$ after Warren's correction for instrumental broadening. K is a constant equal to 0.86 and λ is the wavelength of the X-ray used. β is the effective linewidth of the X-ray reflexion, calculated by the formula $\beta^2 = B^2 - b^2$, where B is the FWHM and b is the instrumental broadening determined by the FWHM of the X-ray reflection of SiO_2, having particles larger than 150 nm, at $2\theta \approx 27°$. Sample compositions were determined by ICP using a P40 atomic adsorption spectrometer from PerkinElmer after dissolution of the catalyst in diluted HCl at 60 °C.

2.3. TPD–TPR characterization

A RXM-100 multi catalyst testing and characterization system (Advanced Scientific Design Inc.) was used to perform oxygen thermodesorption (TPD-O_2) and temperature-programmed reduction (TPR). For TPR experiments, 100 mg of catalysts were placed in a quartz reactor, pretreated under a flow of 20 mL/min (20% O_2 in He) at 550 °C for 2 h and cooled down to room temperature under same composition flow. The TPR-H_2 was carried out under a 10 mL/min flow of 5% H_2 in Ar. The temperature was risen from 25 to 900 °C with a ramp of 5 °C/min. The consumption of hydrogen was monitored and quantified using a TCD. For TPD-O_2 the same pretreatment was performed as for the TPR experiments. The catalysts (100 mg) were submitted to the following conditions: 10 mL/min He, temperature from 25 to 900 °C with a ramp of 5 °C/min. To obtain a complete desorption the catalysts were maintained at 900 °C for 15 min. A TCD was used for the quantification of the oxygen and a mass spectrometer to detect any other desorbing compounds desorption or possible leaks. The amount of oxygen was determined by deconvolution and integration of the desorption profile. To perform a TPD-CH_3OH or TPD-CO_2, two steps were required. During the first step the catalysts (100 mg) were calcined in the same conditions as for TPR experiments. Then the catalysts were treated under 15% CH_3OH in He or under CO_2 at room temperature for 1 h. Thereafter the methanol thermodesorption was carried out under 10 mL/min flow of He from 25 to 900 °C with a ramp of 5 °C/min followed by an isotherm at 900 °C for 15 min. Like TPD-O_2, TCD and mass spectrometer were used to quantify and identify the desorbed species.

2.4. Oxygen storage capacity (OSC) measurements

Oxygen storage capacity (OSC) measurements were performed on the same system as for TPD-O_2 and TPR-H_2 experiments. The catalyst (30 mg) was placed in a U-shaped microreactor, reactant and products were separated on a Porapak Q type column (i.d. = 1 mm, L = 1 m) and analyzed with a TCD. The temperature is set to 500 °C for the four successive steps required for the OSC measurements [20,21]:

(1) a series of O_2 pulses to reach the saturation of the catalyst,
(2) a series of CO pulses until zero conversion of CO or constant CO uptake,
(3) a series of O_2 pulses until complete reoxidation of the solid,
(4) alternated CO–O_2–CO–O_2–CO–O_2 pulses.

The measure of the oxygen storage capacity (OSC value in Table 3) is determined based on the CO uptake during the first CO pulse from the alternated series (step 4). This value corresponds to the amount of highly reactive oxygen which is immediately available for the reaction. The oxygen storage complete capacity (OSCC) is another meaningful measure which represents the total amount of reactive oxygen available for oxidation reactions. This value is determined from the total amount of CO consumed until the end of the CO pulses series (step 2). Since the zero conversion of CO is often not reached at 500 °C, a OSCC-30 value (Table 3) was defined in order to compare the five catalysts under study. Thus this value corresponds to the total amount of CO consumed during the first 30 CO pulses. Finally to evaluate the amount of oxygen in the perovskite lattice ABO_ξ the ξ value is calculated based on the total CO uptake.

2.5. Oxidation reactions

Methanol, methane and carbon monoxide oxidations were performed in a U-shaped quartz reactor (i.d. = 5 mm). The catalytic bed was set up with 100 mg of catalyst inserted between two quartz wool plugs for the three reactions under study. The temperature was controlled using a K-type thermocouple placed in the reactor. In order to purge the catalytic system the catalysts were flushed with a 20 mL/min flow of He for 1 h at room temperature. The feed of methanol oxidation (composed of 0.5% CH_3OH, 20% O_2 in He), methane oxidation (composed of 0.25% CH_4, 20% O_2 in He) and carbon monoxide oxidation (composed of 5% CO, 20% O_2 in He) was passed through the reactor and the temperature was risen. The flow rate was adjusted for each oxidation reactions to 30 mL/min which corresponds to a VHSV of 22500 h^{-1}. Gas samples were collected in the steady state regime at various

reaction temperatures and the products were analyzed with a gas chromatograph (HP 6890 series), equipped with a TCD. Reactants and products were separated using a HayeSep T column (i.d. = 1 mm, L = 2 m × 5 m) for the methanol oxidation and using a Porapak Q type column (i.d. = 1 mm, L = 1 m) for methane and carbon monoxide oxidation.

3. Results

3.1. Physical properties

The chemical composition, BET surface area and crystallite size of the five $La_{1-y}Ce_yCo_{1-x}Fe_xO_3$ perovskites under study are summarized in Table 1. The X-ray diffraction patterns of the five perovskites are shown on Fig. 1. For Co100 and Fe100 the perovskite structure was the only one observed in the XRD diffractograms with their respective crystal structures (rhombohedral for Co100 and orthorhombic for Fe100). For Fe20Co and Fe40Co the perovskite structure was also observed but a distortion from the rhombohedral to the orthorhombic structure was noticed with the increase of the amount of iron in the lattice. No trace of other structure was observed on these four catalysts. Concerning Ce10Co, the intense diffraction peaks attributed to the perovskite structure were observed but a weak signal which corresponds to the CeO_2 structure was also noticed around $2\theta = 27^\circ$.

The five perovskites under study present a specific surface area between 18 m^2/g (Fe100) and 35 m^2/g (Co100). Their particle diameters calculated by the Scherrer equation from XRD lines after Warren's correction for instrumental broadening were found to vary between 9.1 nm (Co100) and 18.2 nm (Fe40Co). A decrease in specific surface area is observed with the increase of the iron substitution in the lattice. This may be related to the structure modification from rhombohedral $LaCoO_3$ to orthorhombic $LaFeO_3$.

Table 1
Physical properties of $La_{1-y}Ce_yCo_{1-x}Fe_xO_3$ catalysts.

Samples	Chemical composition	S_{BET} (m^2/g)	Crystallite size (nm)
Co100	$La_{0.99}Co_{1.02}O_3$	35	9.1
CoFe20	$La_{0.99}Co_{0.81}Fe_{0.20}O_3$	20	16.5
CoFe40	$La_{1.01}Co_{0.61}Fe_{0.39}O_3$	18	18.2
Fe100	$La_{0.99}Fe_{1.01}O_3$	20	17.0
Ce10Co	$La_{0.91}Ce_{0.10}Co_{0.99}O_3$	31	10.8

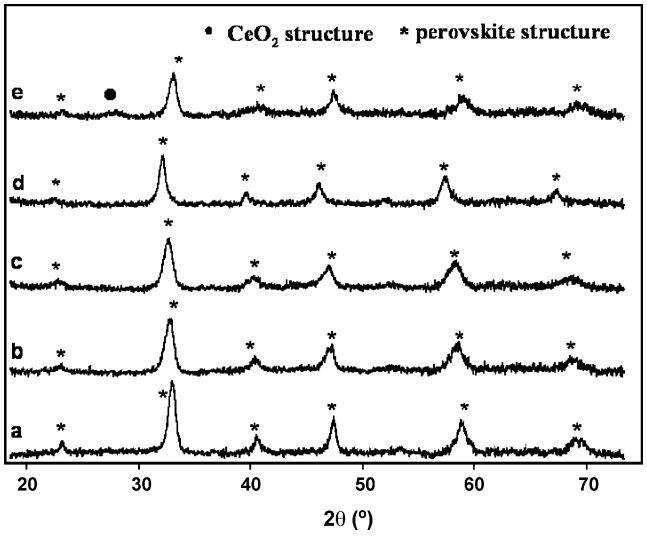

Fig. 1. X-ray diffraction pattern of Co100 (a), CoFe20 (b), CoFe40 (c), Fe100 (d), Ce10Co (e) materials.

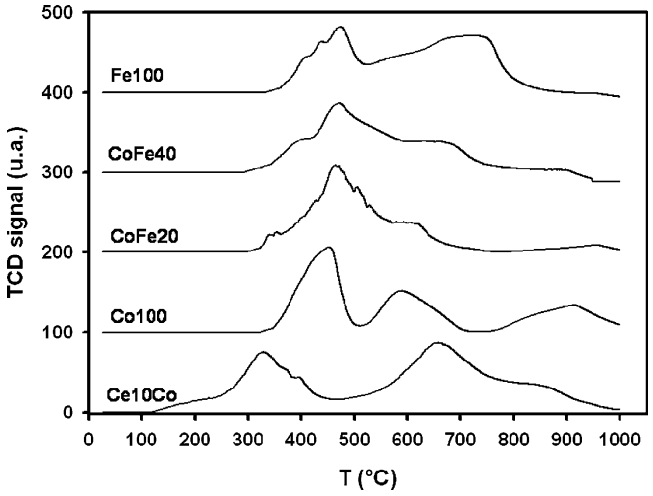

Fig. 2. TPR-H_2 profiles of the $La_{1-y}Ce_yCo_{1-x}Fe_xO_3$ catalysts.

3.2. Temperature-programmed reduction by H_2 (TPR-H_2)

The profiles of the five catalysts under study are presented in Fig. 2 and the results are summarized in Table 2. On each profile, two major signals are observed which correspond to two successive reduction steps. These two steps of reduction were well discussed in the literature. The first signal was ascribed to the reduction of the metallic cation M^{3+} into M^{2+} following the reaction [14,22,23]:

$$LaM^{3+}O_3 + \tfrac{1}{2}H_2 \rightarrow LaM^{2+}O_{2.5} + \tfrac{1}{2}H_2O \quad (1)$$

The second signal was ascribed to the reduction of the M^{2+} into its metallic state M^0 and leads to the destruction of the perovskite structure [24]:

$$LaM^{2+}O_{2.5} + H_2 \rightarrow \tfrac{1}{2}La_2O_3 + M^0 + H_2O \quad (2)$$

For all the catalysts under study the reduction process was found to be over 89% whatever their nature (Table 2). However iron substitution modifies the redox properties of the perovskites since the signals of reduction of each profile were not observed at the same temperature. The temperature of both steps of reduction was found to increase with the increase of the iron substitution. Fig. 2 clearly shows the shift of the two signals to higher temperatures when the content of iron in the structure is increased. The first reduction step on Co100 (Co^{3+} into Co^{2+}) occurs at 460 °C whereas the reduction of the Fe^{3+} into Fe^{2+} on Fe100 required 484 °C (Eq. (1)). The gap of temperature observed concerning the second step of the reduction (M^{2+} into M^0) was even larger than the one observed for the first reduction. Thus on Co100 the complete reduction peaks of the cobalt cation Co^{2+} into its metallic state Co^0 were maximum at 595 °C while the same reaction required 736 °C to complete the total reduction of the iron cation Fe^{2+} into Fe^0 on Fe100 (Eq. (2)). It must be noticed that a small shoulder appears

Table 2
Temperature-programmed reduction by H_2 on $La_{1-y}Ce_yCo_{1-x}Fe_xO_3$ catalysts.

Samples	Reduction temperature (°C)		Reduction[a]
	Peak 1 (M^{3+} to M^{2+})	Peak 2 (M^{2+} to M^0)	M^{3+} to M^0 (%)
Co100	460	595	94
CoFe20	475	615	89
CoFe40	480	655	89
Fe100	484	736	93
Ce10Co	315	668	96

[a] At the end of the TPR-H_2 experiment.

before the first signal of reduction, in Fig. 2, on each profile of iron containing perovskites. This may indicate the presence of a small amount of Fe^{4+} species as previously reported in the literature [25] and in our previous works where an excess of H_2 consumed during the first step of reduction was measured [14,26].

The insertion of Ce in the $LaCoO_3$ perovskite structure also induces some modifications of its redox behaviour. Thus the partial substitution of 10% of La by Ce in cobaltite lattice (Ce10Co) leads to an easier reducibility of the Co^{3+} into Co^{2+} since this reduction step occurs at lower temperatures (315 °C) on Ce10Co in comparison with 460 °C on Co100 (Fig. 2). Surprisingly, the second reduction (Co^{2+} into Co^0) was found to be more difficult since the second signal was shifted to higher temperature on Ce10Co compared to Co100.

3.3. OSC measurements

The oxygen storage capacity measurement is usually performed to quantify the amount of oxygen available for a reaction at a given temperature [20,21]. The OSC measurements were carried out at 500 °C on each catalyst. According to the TPR-H_2 experiments, this temperature corresponds to the end of the first signal of reduction [20]. The oxygen storage capacity of a perovskite was found to be highly dependant on its nature. Indeed, the measures summarized in Table 3 clearly show the decrease of the OSC value after one CO pulse with the increase of the iron substitution. The OSC was even found to be nearly twice higher on Co100 (418 μmol/g) in comparison with Fe100 (195 μmol/g). All along the thirty CO pulses, the OSC value, evaluated after each pulse, decreases until it becomes almost constant around the twentieth pulse on Fe20Co, Fe40Co and Fe100 and after the twentyfifth pulse on Co100 (Fig. 3). Thus, after thirty CO pulses the cumulative OSC (OSCC-30) of the Co100 catalyst represents 3361 μmol/g and still decrease with the increase of the iron substitution to reach 1402 μmol/g for Fe100.

Table 3
OSC measurements on $La_{1-y}Ce_yCo_{1-x}Fe_xO_3$ catalysts.

Samples	ξ (ABO_ξ)	OSC (μmol/g)	ξc-30 (ABO_ξ)[a]	OSCC-30[a] (μmol/g)
Co100	2.89	418	2.17	3361
CoFe20	2.91	375	2.48	2097
CoFe40	2.93	265	2.56	1799
Fe100	2.95	195	2.65	1402
Ce10Co	2.89	446	2.30	2828

[a] ξc-30 and OSCC-30 represent the cumulative values after 30 CO pulses.

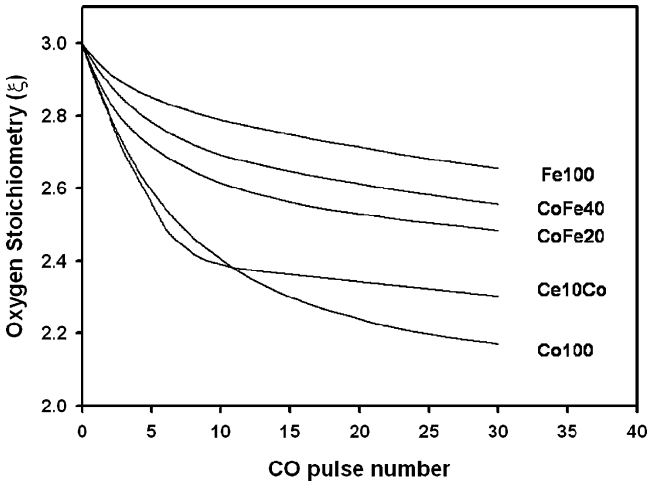

Fig. 3. Evolution of the oxygen content in the perovskite lattice (ξ) during the CO pulses.

The residual oxygen stoichiometries after thirty CO pulses (ξc-30) correspond respectively to 2.17 and 2.65 for Co100 and Fe100 perovskites. Due to a residual stoichiometry lower than 2.5 on Co100 ($LaCoO_{2.17}$ after 30 CO pulses) and CoFe20 ($LaFe_{0.20}Co_{0.80}O_{2.48}$ after 30 CO pulses) the OSC measurements indicate that a non negligible amount of the cobalt was reduced from Co^{3+} into Co^0 since the first step of the reduction. Such observation is in accordance with previous studies of our laboratory [26,27].

The partial substitution of lanthanum by cerium (Ce10Co) leads to a small gain of 28 μmol/g on the OSC value in comparison with Co100. However the profiles of the evolution of oxygen stoichiometry all along the reaction, in Fig. 3, show a large difference between Co100 and Ce10Co catalysts. A slightly faster reduction was observed on Ce10Co at the begining of the OSC process in comparison with Co100. However the conversion of the CO pulses on Ce10Co rapidly decreases after 8 pulses until it becomes constant and finally reaches an OSCC-30 value of 2828 μmol/g and a residual formula of $La_{0.90}Ce_{0.10}CoO_{2.30}$ after 30 pulses. Finally in spite of a small gain of 28 μmol/g on the OSC value the Ce10Co catalyst presents a deficit of 533 μmol/g in comparison with the Co100 catalyst at the end of the OSC process.

3.4. Temperature-programmed desorption of O_2 (TPD-O_2)

The TPD-O_2 experiments on the five catalysts under study show two kinds of desorbed oxygen which correspond to two peaks on the profiles (Fig. 4). These two types of oxygen are widely reported in the literature and are differentiated by their temperatures of desorption. The first kind is designated as α-O_2 and it desorbs generally below 700 °C. It is considered as a surface species [13] and its desorption is represented by Eq. (3):

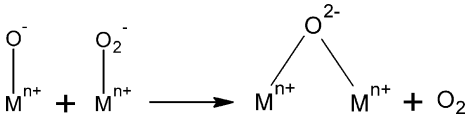

(3)

or Eq. (4):

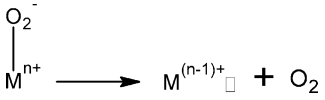

(4)

The desorption temperature of α-O_2 is strongly dependant on the temperature of calcination so that when calcination is performed at 550 °C oxygen desorption peaks are observed at

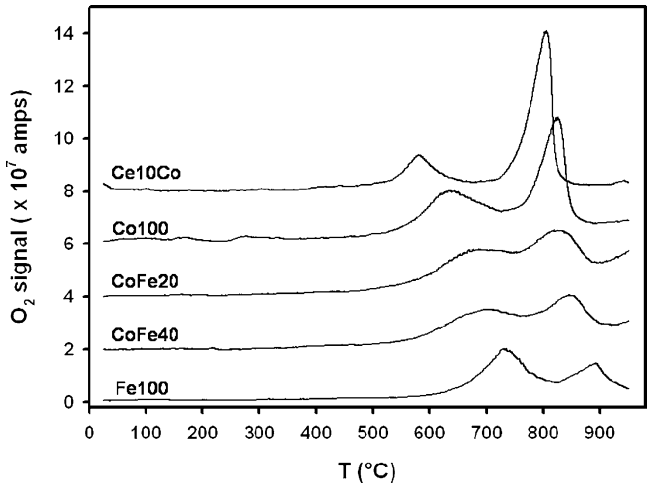

Fig. 4. TPD-O_2 profiles of the $La_{1-y}Ce_yCo_{1-x}Fe_xO_3$ catalysts.

Table 4
Amounts of oxygen desorbed during the TPD-O_2 experiments on $La_{1-y}Ce_yCo_{1-x}Fe_xO_3$ catalysts.

Samples	T (°C)		Amount of oxygen desorbed (mmol/g)[a]		Amount of monolayers desorbed[b]	
	α	β	α	β	α	β
Co100	638	826	165	470	1.18	3.36
CoFe20	690	832	87	239	1.08	2.99
CoFe40	709	850	74	159	1.03	2.21
Fe100	735	895	85	66	1.06	0.83
Ce10Co	584	807	121	634	0.98	5.11

[a] Calculated by deconvolution from the TCD signal.
[b] Calculated by assuming 4 μmol/m^2 for one monolayer.

600–650 °C. At these temperatures it is very likely that the molecular O_2^- species dissociate into atomic species. However since this dissociation is reversed during the desorption process, the α-O_2 desorption may still be depicted by Eq. (3) or (4). Fig. 4 clearly shows a wide range of temperature for the α-O_2 desorption of the five $La_{1-y}Ce_yCo_{1-x}Fe_xO_3$ perovskites from 584 °C on Ce10Co to 735 °C on Fe100. A shift towards higher temperatures was even observed with the increase of the iron insertion. Thus the α-O_2 desorption temperature was found to increase in the following order: Ce10Co < Co100 < CoFe20 < CoFe40 < Fe100. The amounts of α-O_2 desorbed was measured by deconvolution of the O_2 desorption curves using Lorentzian peak shapes in a computer peak-fitting routine. In terms of monolayer (assuming that one monolayer of oxygen is equal to 4 μmol/m^2) the amount of α-O_2 desorbed was found to be equivalent to one or slightly over one monolayer for each of the five perovskites under study (Table 4).

The second peak detected, above 750 °C on each profiles, is ascribed to the β-O_2 which originates from the bulk of the structure and is often considered as an indicator of the mobility of the oxygen in the structure. This desorption requires the formation of β-O_2 desorption site [13]:

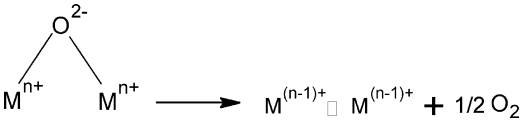

(5)

This step is followed by the diffusion of β-oxygen from the bulk to the desorption site at the surface of the structure:

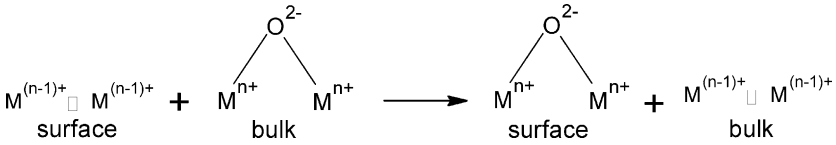

(6)

A large difference was also observed concerning the temperature of desorption for the β-O_2 from the bulk of the structure. Indeed the lowest temperature observed for the desorption of those oxygens was on Ce10Co at 807 °C in comparison with the highest one on Fe100 at 895 °C. Moreover the same kind of shift towards higher temperatures was noticed with the increase of the iron in the lattice and the same order for the β-O_2 desorption temperature was observed: Ce10Co < Co100 < CoFe20 < CoFe40 < Fe100. However the amount of β-O_2 desorbed was found to be strongly dependant on the nature of the perovskite (Table 4). Thus the presence of cerium improves the oxygen mobility in the bulk since 634 μmol/g of β-O_2 were desorbed on Ce10Co whereas 470 μmol/g were measured on Co100. Unlike cerium, iron induces an inhibition effect on the oxygen mobility in the lattice as shown in Table 4. Indeed the amount of β-O_2 was found to decrease as the content in iron in the perovskite increases and only 66 μmol/g of β-O_2 were desorbed from the Fe100 perovskite.

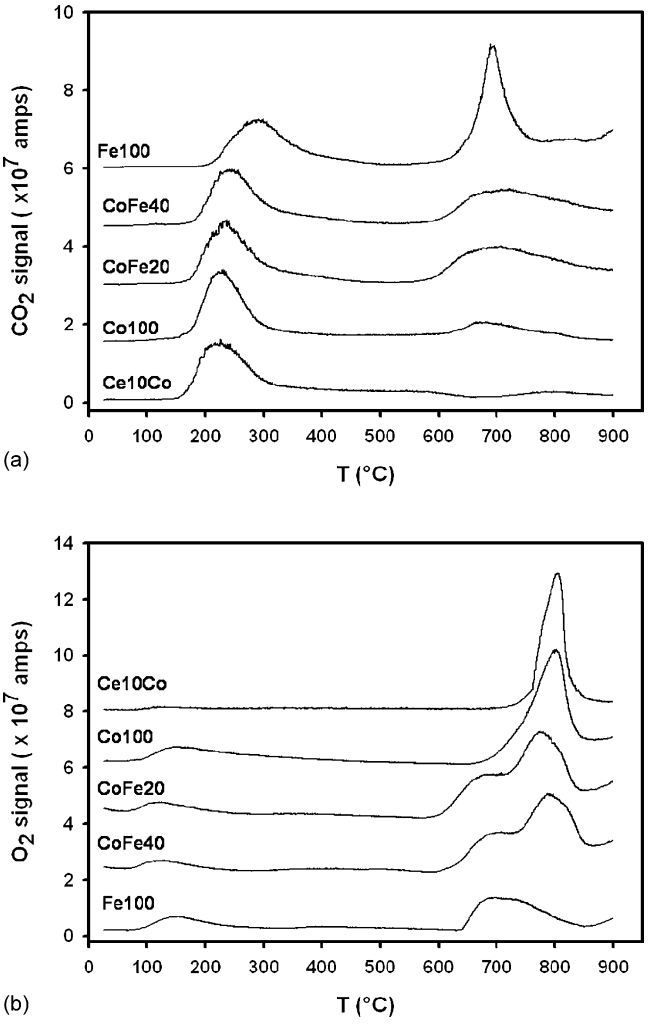

Fig. 5. TPD-CH_3OH profiles of the $La_{1-y}Ce_yCo_{1-x}Fe_xO_3$ catalysts, CO_2 signal (a), O_2 signal (b).

3.5. Temperature-programmed desorption of CH_3OH (TPD-CH_3OH)

The desorption signals of CO_2 ($m/z = 44$) and O_2 ($m/z = 32$) during the TPD-CH_3OH experiments for the five catalysts under study are shown in Fig. 5a and b and Table 5. The desorption signal of methanol ($m/z = 31$) is not shown since only one peak corresponding to physisorbed methanol desorption was observed around 125 °C for each of the catalysts studied.

The CO_2 desorption curves, presented in Fig. 5a, show two significant peaks on most of the five profiles. The first signal was detected on each catalyst but with a slight difference in desorption temperature, with these temperatures being in the following

Table 5
Results of the TPD-CH_3OH experiments obtained on $La_{1-y}Ce_yCo_{1-x}Fe_xO_3$ catalysts.

Samples	Amount of O_2 desorbed, μmol/g (T_{max}, °C)[a]		Relative amount of CO_2 desorbed, % (T_{max}, °C)[a]	
	α	β	Peak 1	Peak 2
Co100	–	457 (806)	94 (232)	6 (682)
CoFe20	33 (688)	231 (780)	60 (240)	40 (701)
CoFe40	31 (702)	158 (792)	56 (247)	44 (704)
Fe100	54 (695)	47 (790)	35 (293)	65 (696)
Ce10Co	–	621 (807)	100 (225)	–

[a] Calculated by deconvolution from the TCD signal.

order: Ce10Co (225 °C) < Co100 (232 °C) < CoFe20 (232 °C) < CoFe40 (240 °C) < Fe100 (293 °C). These signals are ascribed to the desorption of the monodentate carbonates formed after total oxidation of adsorbed methanol into CO_2. Similar peaks were previously observed on other kinds of perovskites in our previous works [26,28]. A second peak centered around 700 °C appears on each profile, except on Ce10Co. By contrast with the first signal, this one is due to the desorption of the bidentate carbonates which are more stable than the monodentate carbonates and require higher temperatures to desorb [26,28]. Furthermore the relative abundance of the two peaks were determined for each catalyst and summarized in Table 5. These values indicate that the content of iron influences the relative formation of bidentate carbonates compared to monodentate carbonates.

The signal of oxygen was also monitored during the TPD-CH_3OH experiments (Fig. 5b). A small signal was observed above 200 °C on each profile, which is obviously due to the parent peak of CH_3OH. For the three catalysts which contain iron (CoFe20, CoFe40 and Fe100), the same kind of pattern was observed as the ones obtained during TPD-O_2 experiments. However a modification of the desorption temperatures must be noticed. The α-O_2 signals were in this case detected at lower temperature than during the TPD-O_2 experiments and were found to desorb at the same temperature as the CO_2 generated from the bidentate carbonates (around 700 °C). Moreover the same observation in terms of temperature was noticed for the β-O_2 desorption. On Co100 and Ce10Co catalysts, no desorption signal of the α-O_2 was detected and a decrease of the desorption temperature of the β-O_2 was also noticed. Table 5 shows the consumption of the α-O_2 for the five perovskites under study whereas the amount of β-O2 desorbed was found to be barely equivalent to the amount desorbed during the TPD-O_2 experiments.

3.6. Catalytic activity in VOC oxidation

The activity in oxidation of the five perovskites under study was evaluated for three different reactions. The results are shown in Figs. 6–8 and the T_{50} and T_{100} values are summarized in Table 6.

3.6.1. CH_3OH oxidation

Among the five perovskites under study, the Ce10Co catalyst presents the highest efficiency for the methanol oxidation (Fig. 6).

Table 6
Results of the CH_3OH, CO, CH_4 oxidations.

Samples	CH_3OH		CO		CH_4	
	$T_{50\%}$ (°C)	$T_{100\%}$ (°C)	$T_{50\%}$ (°C)	$T_{100\%}$ (°C)	$T_{50\%}$ (°C)	$T_{100\%}$ (°C)
Ce10Co	112	142	85	104	365	438
Co100	154	195	162	229	418	519
CoFe20	171	231	237	331	479	614
CoFe40	191	256	256	371	540	687
Fe100	209	287	342	–	595	784

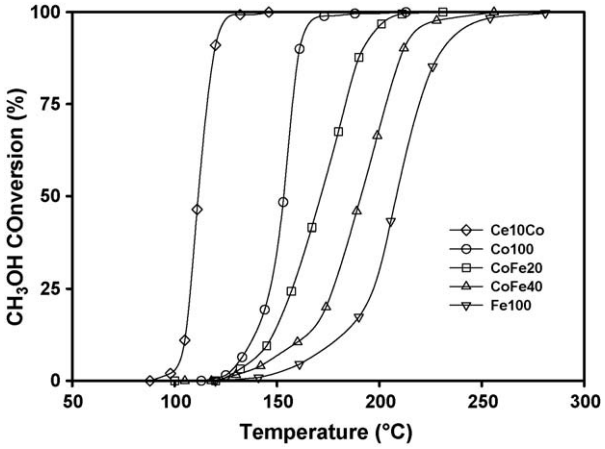

Fig. 6. Steady state oxidation of CH_3OH over $La_{1-y}Ce_yCo_{1-x}Fe_xO_3$ catalysts.

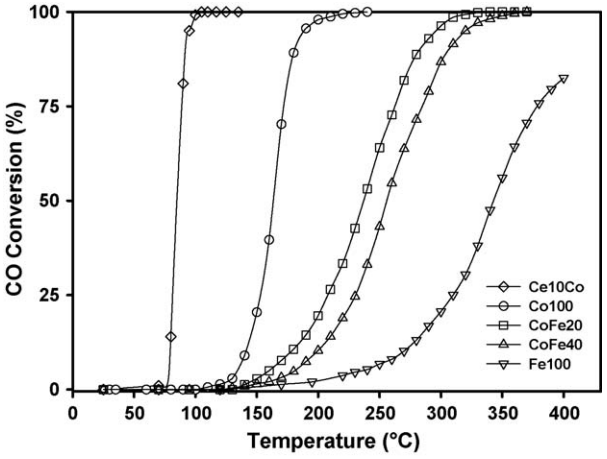

Fig. 7. Steady state oxidation of CO over $La_{1-y}Ce_yCo_{1-x}Fe_xO_3$ catalysts.

The total conversion into CO_2 was achieved at 142 °C whereas at the same temperature the conversion measured on Co100 catalyst only reaches 20%. Fig. 6 also shows that the efficiency of the catalysts decreases with the increase in iron content. The methanol oxidation is not only slowed down at low temperatures but reaching the complete conversion also requires higher temperature. A difference of around 60 °C was observed between the Co100 (154 °C) and the Fe100 (209 °C) catalysts at 50% of conversion and this difference reaches close to 100 °C at 100% of conversion on the

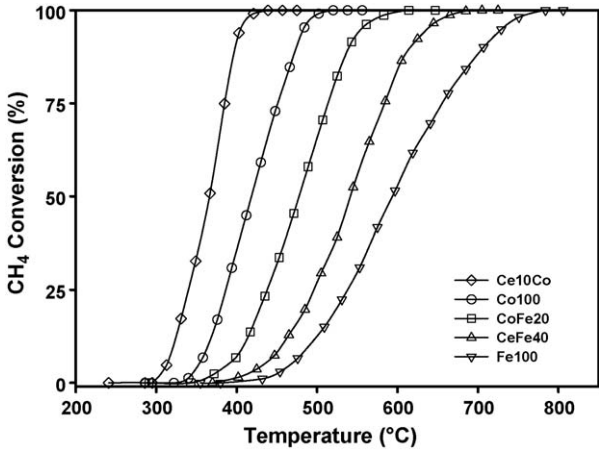

Fig. 8. Steady state oxidation of CH_4 over $La_{1-y}Ce_yCo_{1-x}Fe_xO_3$ catalysts.

same catalysts (Co100: 195 °C, Fe100: 287 °C). Thus the efficiencies of the five perovskites under study for this reaction are ranked in the following order: Ce10Co > Co100 > CoFe20 > CoFe40 > Fe100. It must be noticed that no other product than CO_2 was observed on each catalyst for the methanol oxidation reaction (limit of detection for formaldehyde 10 ppm).

3.6.2. CO oxidation

The CO oxidation results on the $La_{1-y}Ce_yCo_{1-x}Fe_xO_3$ catalysts are plotted in Fig. 7. As for the methanol oxidation the Ce10Co catalyst displays the highest efficiency for the CO oxidation. A large difference was even observed between Ce10Co and Co100 since at 105 °C the CO oxidation is completed on Ce10Co whereas on Co100 the CO conversion is still zero. For this reaction the increase in iron substitution was also found to induce a decrease in oxidation activity. Indeed the begining of the CO oxidation was severely slowed down as the content in iron increased (Fig. 7). As a consequence the total CO oxidation was observed to be complete at 331 °C on CoFe20 and 371 °C on CoFe40 in comparison with 229 °C on Co100. On the Fe100 catalyst the conversion into CO_2 was even found incomplete at 400 °C. Like for the methanol oxidation, CO_2 was the only product observed during CO oxidation.

3.6.3. CH_4 oxidation

The methane oxidation reaction occurs at higher temperature but the results, shown on Fig. 8, are similar to those for CO and CH_3OH oxidation reactions. The five catalysts under study are ranked in the same order in terms of efficiency: Ce10Co > Co100 > CoFe20 > CoFe40 > Fe100. The temperature scale for complete methane oxidation was observed from 438 °C on Ce10Co to 784 °C on Fe100. Like for the previous oxidation reactions, the increase in iron content leads to a slowdown of the activity at the begining of the methane oxidation on CoFe20, CoFe40 and Fe100 catalysts.

4. Discussion

The TPR-H_2 profiles clearly indicate the major effect of the composition of the perovskites on their reducibility. Even if the five perovskites under study reach total reduction of the transition cation up to the metallic state (M^0), some differences were observed. Thus a large difference in temperature was noticed for the first oxidation step between Ce10Co and Co100 catalysts. In accordance with Eq. (1), this indicates that the insertion of cerium in the perovskite lattice leads to an easier reducibility of Co^{3+} into Co^{2+}. Such information was also confirmed by the OSC measurements since the OSC value after one pulse is higher on Ce10Co (446 μmol/g) than on Co100 (418 μmol/g). However for the second step of the reduction (Eq. (2)) an increase of the temperature was observed for Ce10Co in comparison with Co100. The effect of the iron content in the perovskite lattice on its reducibility was plotted in Fig. 9. It was observed that the iron content induces only a minor effect on the reduction of M^{3+} into M^{2+} since only low variations of the temperature of the first peak can be noticed in the TPR-H_2 profiles. However a strong influence is induced by the iron substitution on the temperature of the second step of the reduction which leads to the metallic state of the B-site cation.

These TPR-H_2 results may indicate a more complex reduction mechanism than the simple two steps mechanism usually cited in the literature. Moreover the residual oxygen stoichiometry, obtained after 30 CO pulses during the OSC experiments at 500 °C, below 2.5 on Co100, Ce10Co and CoFe20 catalysts, clearly corroborates this hypothesis. In accordance with previous studies it is likely that a fraction of the B-site cations is reduced into its metallic state at the end of the first reduction step [14,27].

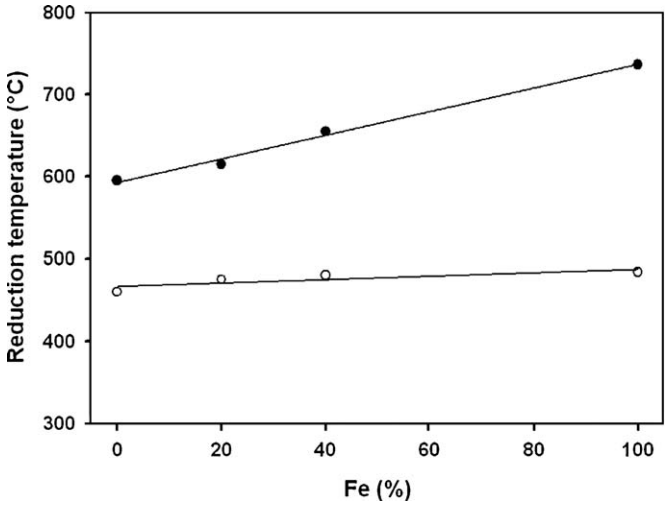

Fig. 9. Correlation between the amount of iron in the structures and the temperature reduction obtained during TPR-H_2 (○: low T signal; ●: high T signal).

The TPD-O_2 experiments show two kinds of oxygens as usually observed by several authors for numerous perovskites. No real influence of the nature of the A- or B-site cation was observed on the amount of α-O_2 desorbed. Indeed for the five perovskites under study this quantity was found to be equal to approximately one monolayer on each catalyst. These results validate the accepted view that α-O_2 are weakly linked or chemisorbed on the accessible surface of the perovskites. However the desorption temperature of α-O_2 seems to be related with the nature of the B-site cation and more particularly with the iron substitution. Fig. 10 clearly shows the correlation between this temperature and the average electronegativity of the transition metal in B position. In our previous work, the electronegativity of the A-site cation in $AMnO_3$ was identified as the major parameter to explain some observed shifts of the α-O_2 desorption temperature [28]. It was found that the α-O_2 desorption temperature increases for the less electronegative rare earths. Such model seems to be applicable to the present system since an increase of the iron substitution leads to a decreased global electronegativity of the perovskite and therefore to an increase of the α-O_2 desorption temperature. The electronegativity also allows to explain the decrease of the desorption temperature of the oxygen on the Ce10Co in comparison with Co100 since the electronegativity of the cerium is higher than the one of the lanthanum. Moreover, due to the higher coordination of

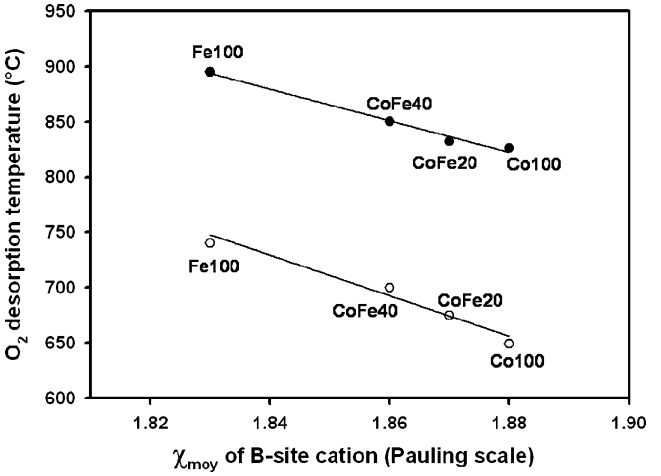

Fig. 10. Correlation between the average B-site cations electronegativity and the oxygen temperature desorption obtained during TPD-O_2 (○: α-O_2; ●: β-O_2).

the A-site cations in comparison with the B-site cations, the decrease of the desorption temperature of α-O_2 is more affected in this case in spite of a weaker electronegativity difference between lanthanum and cerium. Concerning the oxygen originating from the bulk of the perovskite (β-O_2), Fig. 10 also shows that the electronegativity affects their desorption temperature in the same way as for the α-O_2.

Finally, it appears that the amount of β-O_2 is strongly related with the nature of the A- and B-site cations. Thus increasing the iron content in the perovskite lattice leads to a drastic decrease of the amount of β-O_2 until almost zero on Fe100 (Table 4) as opposed to the cerium substitution which induces a large gain in β-oxygen.

The TPD-CH_3OH profiles indicate the formation of two kinds of carbonate species on most of the catalysts. With the exception of Ce10Co, these two types of carbonates lead to the desorption of CO_2 as two distinct signals, one below 300 °C and the other above 650 °C. In accordance with our previous studies these CO_2 desorptions occur with the following mechanisms [26,28]:

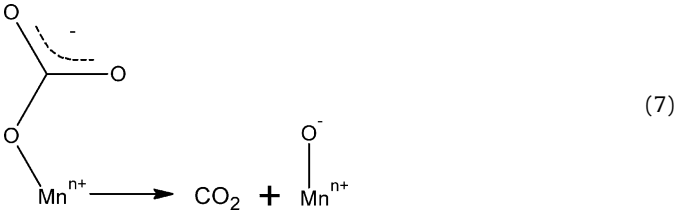

(7)

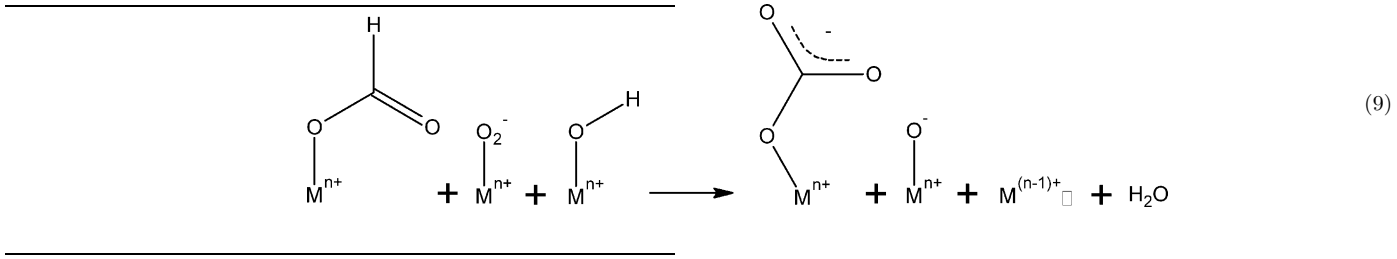

(9)

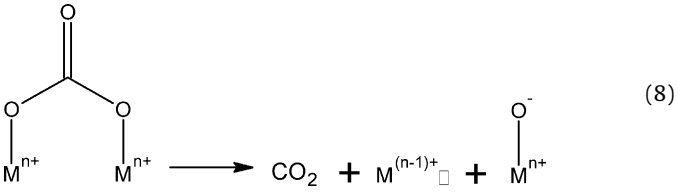

(8)

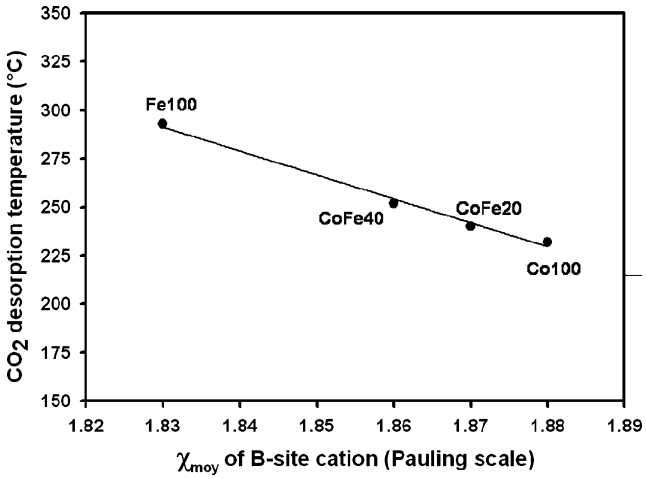

Fig. 11. Correlation between the average B-site cations electronegativity and the CO_2 temperature desorption (monodentate species) obtained during TPD-CH_3OH.

As opposed to the desorption temperature of the bidentate carbonate (Eq. (8)), which does not seem to be affected by the nature of the A- and B-site cations, the desorption of the monodentate carbonate (Eq. (7)) is strongly correlated to the electronegativity of the cation in the perovskite lattice (Fig. 11). Thus the modification of the nature of the surface induces a change in the active sites basicity, which modifies the desorption temperature of the monodentate carbonates. Increasing the electronegativity difference between the cation and the oxygen anion of the bond M^{n+}–O, indeed leads to an increase of the partial negative charge on the oxygen which makes the active site more basic. Then the perovskite with the most basic surface (Fe100) leads to the formation of the most stable monodentate carbonates. Such changes in the nature of the surface also seem to impact the relative amount of CO_2 desorbed during TPD-CH_3OH since the relative amount of bidentate carbonates increases with the increase of the iron substitution (Table 5). By comparing the O_2 signals of the TPD-CH_3OH (Fig. 5b) to the ones of TPD-O_2 (Fig. 4) a consumption of α-O2 was observed after CO_2 desorption, which indicates the nature of the reactive oxygen. However it is surprising to note that all the α-O_2 of the three catalysts containing iron (CoFe20, CoFe40 and Fe100) have not been totally consumed. At the same time on these three catalysts a massive signal ascribed to the bidentate carbonates has been detected during the TPD-CH_3OH experiments (Fig. 5a). Based on a methanol oxidation mechanism proposed in our previous works, the formation of the monodentate carbonate was assumed to occur according to reaction (9) [26,28]:

The $M^{n+}O_2^-$ was identified as the reactive oxygen species, then in case of a lack of this species at the surface of the perovskite a second reaction would take place. Reaction (10) then leads to the formation of strongly adsorbed bidentate carbonate which requires a high temperature (above 680 °C) to desorb:

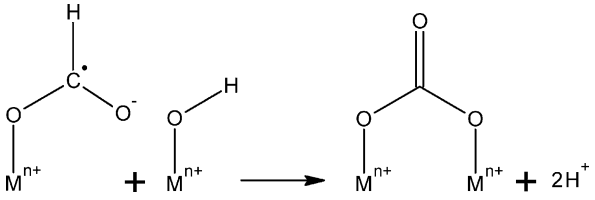

(10)

Based on this mechanism, two hypotheses may explain the production of bidentate carbonates on CoFe20, CeFe40 and Fe100 catalysts in spite the presence of residual α-O_2 observed during TPD-CH_3OH experiments and the differences in the carbonates distribution signals:

(1) The residual α-O_2 observed in the O_2 profile recorded during the TPD-CH_3OH might correspond to a non-reactive fraction of the surface oxygen. Thus after the total uptake of the $M^{n+}O_2^-$ species for the production of monodentate carbonates (Eq. (9)), the bidentate carbonates are formed (Eq. (10)). In this case, Eqs. (9) and (10) are successive.
(2) Iron cations might preferentially lead to the formation of bidentate carbonate (Eq. (10)), due to its low electronegativity

and the strong basicity of the surface of the catalysts. In this case, Eqs. (9) and (10) are in competition and the residual amount of α-O_2 unused for the oxidation was observed due to the ability of the iron cation to orient the mechanism towards Eq. (10).

Concerning the β-O_2 desorbed during TDP-CH_3OH, its amount is close to the one observed during the TPD-O_2. Small differences were however observed in desorption temperature.

Total methanol oxidation was found to be highly affected by the specific surface area (S_{BET}), the reducibility of the B-site cation and by the α-oxygen density [26]. Thus the larger difference in activity of the Ce10Co catalyst in comparison with the four other perovskites under study (Fig. 6) must be a direct consequence of its high reducibility at low temperature (Fig. 2) since this catalyst does not display the highest S_{BET} and α-O_2 density. However intrinsic redox properties are not enough to explain the differences observed in the catalytic activity for the methanol oxidation on the Co100, CoFe20, CoFe40 and Fe100 catalysts since only small differences are observable during TPR-H_2 on these catalysts. It was observed in Fig. 6, that an increase of the iron content leads to a slowdown of the catalytic activity. Such an observation is in accordance with the second hypothesis according to which monodentate carbonate desorbing according to Eq. (10) becomes paramount in comparison to Eq. (9), when iron substitution increases. In this situation the production of bidentate carbonates, which requires a high temperature to desorb, leads to a blocking of the active site and thus a slowdown of the methanol oxidation reaction at low temperature.

CO oxidation is well known to occur according to a suprafacial mechanism [29]. In this mechanism, the active oxygen is supposed to be a dissociatively adsorbed oxygen (O^-) which reacts with adsorbed CO. In this condition the specific surface area was identified as one of the major parameters for this oxidation reaction. Surprisingly and as it was observed in the case of the methanol oxidation, our results cannot be correlated with the specific surface area of the five perovskites under study since the most efficient catalyst (Ce10Co) does not display the highest S_{BET}. However a good correlation is observed between the efficiency of the catalysts for the CO oxidation and the reducibility results obtained during OSC and TPR-H_2 experiments. This indicates that the modification of the surface reactivity induced by increasing the iron content in the perovskite largely affects the CO oxidation rate at low temperature. Moreover, the formation of carbonates as a result of CO oxidation has been proposed by Tascon et al. [30]. It is thus conceivable, based on our hypothesis, that like methanol oxidation, the formation of bidentate carbonate might become paramount compared to the monodentate carbonate and consequently cause the slow activity at the begining of the reaction.

Like for the other two reactions, the iron also leads to a loss in catalytic activity for methane oxidation. However due to the higher temperature required to achieved this reaction, the formation of bidentate carbonates cannot explain the lower activity of the perovskite containing iron. Several authors indicated that morphology is an important factor towards the methane oxidation [14,31]. Our results show that the S_{BET} does not correlate very well with activity. This observation is particularly true when comparing Ce10Co and Co100 catalysts since the first one is more active than the second although it has a lower specific surface area. A remarkable relation between the amount of β-O_2 available and the temperature of 50% and 100% of methane conversion has been established in Fig. 12. This clearly indicates that the mobility of the oxygen in the bulk of the structure largely affects the activity of the solid in methane oxidation reaction. Thus iron, by limiting the oxygen transfer from the bulk to the surface, slows the reoxidation of the active sites from M^{2+} into M^{3+} following a Mars–Van-

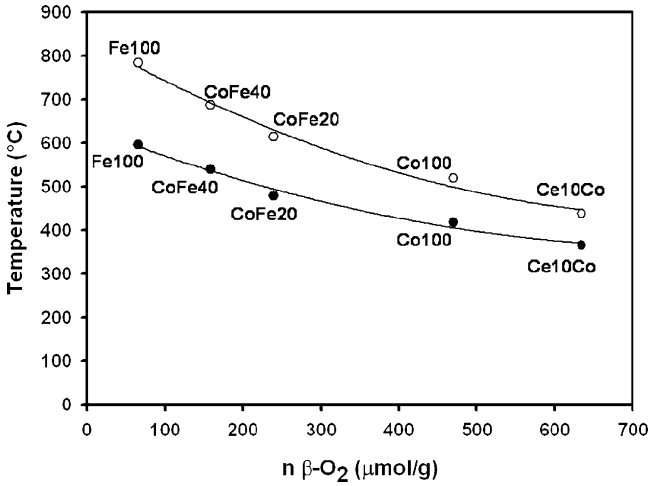

Fig. 12. Correlation between the amount of β-O_2 desorbed during TPD-O_2 and oxidation temperature of CH4 conversion of T_{50} (●) and T_{100} (○).

Krevelen mechanism. In these conditions the mobility of the oxygen in the perovskite lattice as represented by the amount of β-O_2 desorbed during TPD-O_2, is considered as one of the major parameters of the CH_4 oxidation reactions. This is in accordance with our previous studies in methane oxidation [13–15]. However, the electronegativity of the A- or B-site cations may have a role in the release of the β-O_2 from the lattice of the perovskite. In these conditions, any increase of the electronegativity difference between A- or B-site cation and oxygen leads to an increase of the breaking bond energy of the A^{n+}/B^{n+}–O. Thus any increase of the iron substitution induces a decrease of the β-O_2, due to the lower electronegativity of iron in comparison with cobalt, and consequently leads to a constant decrease of the methane oxidation activity on these catalysts. On the contrary, the addition of cerium, which displays a slightly higher electronegativity than lanthanum, enables a gain in β-O_2 which allows the methane oxidation at rather low temperatures [18].

5. Conclusion

The substitution of the A- or B-site cations in the perovskite lattice leads to strong modifications of their redox behaviours. The study of the reducibility of the perovskites by TPR-H_2 clearly indicates two different reduction steps. The first one seems to be more impacted by cerium substitution than iron substitution. However a large impact on the reduction into the metallic state of the B-site cations has been observed. It appears that the reduction into Fe(0) occurs at higher temperature than the reduction into Co(0). However, the OSC measurements also show that the mechanism which rules the reduction of the transition metal is more complex than the simple two steps mechanism usually reported.

The two kinds of oxygen usually reported in perovskite lattice during the TPD-O_2 experiments were found to be highly related with the electronegativity of the A- and B-site cations. A linear correlation was even found between the average electronegativity of the A- and B-site cations and both the desorption temperature and the amount of β-O_2 desorbed. A similar correlation of the electronegativity with the desorption temperature of carbonates has been observed during the TPD-CH_3OH.

Due to the low temperature at which CO and CH_3OH oxidations occur, some similarities in the mechanism have been observed. The reducibility and α-O_2 density of the perovskites were determined as the major parameters in these two reactions. Thus it is suggested that the formation of bidentate carbonates, which become

paramount after consumption of reactive surface oxygen, may lead to a slowdown of the oxidation activity. This is particularly the case when the iron substitution increases in the catalyst.

For methane oxidation, the activity was found to be directly linked with of the amount of β-O_2 and consequently to the electronegativity of the A- and B-site cations. Thus with a small electronegativity gap between A-/B- site cations and oxygen (like in the case of Fe100) the desorption of β-O_2 is limited and the activity of this catalyst is weak. This is in contrast to perovskites composed with lower A-/B-site cations electronegativity (like in the case of Ce10Co and Co100) which display higher efficiency in CH_4 oxidation corresponding to the higher amount of β-O_2 desorbed during TPD-O_2.

Acknowledgements

Nanox Inc. (Québec, Canada) and Prof. H. Alamdari are acknowledged for the preparation of the samples. The financial contribution of the Natural Sciences and Engineering Research Council of Canada, through an industrial chair, is gratefully acknowledged.

References

[1] V.M. Goldschmidt, Akad. Oslo J. Mat. Nat. 2 (1926) 7.
[2] W.F. Libby, Science 171 (1971) 499.
[3] R.J.H. Voorhoeve, J.P. Remeika Jr., P.E. Freeland, B.T. Mathias, Science 177 (1972) 353.
[4] R.J.H. Voorhoeve, D.W. Johnson, J.P. Remeika, P.K. Gallagher, Science 195 (1977) 827.
[5] R.J.H. Voorhoeve, in: H.H. Burton, R.L. Garden (Eds.), Advanced Materials in Catalysis, Academic Press, New York, 1977, p. 127.
[6] L.G. Tejuca, J.L.G. Fierro, Properties and Applications of Perovskite-Type oxides, Dekker, New York, 1993.
[7] H. Arai, T. Yamada, K. Eguchi, T. Seiyama, Appl. Catal. 26 (1986) 265.
[8] P.K. Gallagher, Mater. Res. Bull. 3 (1967) 225.
[9] H.-M. Zhang, Y. Teraoka, N. Yamazoe, Chem. Lett. (1987) 665.
[10] J. Kirchnerova, D. Klvana, Int. J. Hydrogen Energy 19 (1994) 501.
[11] R.A.M. Giacomuzzi, M. Portinari, I. Rossetti, L. Forni, Stud. Surf. Sci. Catal. 130 (2000) 197.
[12] S. Kaliaguine, A. van Neste, US Patent 6017504 (2000).
[13] S. Kaliaguine, A. van Neste, V. Szabo, J.E. Gallot, M. Bassir, R. Muzychuk, Appl. Catal. A 209 (2001) 345.
[14] S. Royer, F. Bérubé, S. Kaliaguine, Appl Catal. A 282 (2005) 273.
[15] S. Royer, D. Duprez, S. Kaliaguine, J. Catal. 234 (2005) 364.
[16] T. Nitadori, M. Misono, J. Catal. 93 (1985) 459.
[17] L. Forni, C. Oliva, F.P. Vatti, M.A. Kandala, A.M. Ezerets, A.V. Vishniakov, Appl. Catal. B: Environ. 7 (1996) 269.
[18] M. Alifanti, R. Auer, J. Kirchnerova, F. Thyrion, P. Grange, B. Delmon, Appl. Catal. B: Environ. 41 (2003) 71.
[19] B. Bialobok, J. Trawczynski, W. Mista, M. Zawadzki, Appl. Catal. B: Environ. 72 (2007) 395.
[20] S. Royer, H. Alamdari, D. Duprez, S. Kaliaguine, Appl. Catal. B 58 (2005) 275.
[21] S. Royer, B. Levasseur, H. Alamdari, J. Barbier Jr., D. Duprez, S. Kaliaguine, Appl. Catal. B: Environ. 80 (2008) 51.
[22] A. Baiker, P.E. Martin, P. Keusch, E. Fritsch, A. Reller, J. Catal. 146 (1) (1994) 268.
[23] J.L.G. Fierro, M.A. Pena, L.G. Tejuca, J. Mater. Sci. 23 (1998) 1018.
[24] M. Crespin, W.K. Hall, J. Catal. 69 (1981) 359.
[25] P. Ciambelli, S. Cimino, L. Lisi, M. Faticanti, G. Minelli, I. Pettiti, P. Porta, Appl. Catal. B 33 (2001) 193.
[26] B. Levasseur, S. Kaliaguine, Appl. Catal. A 343 (2008) 29.
[27] B. Echchahed, H. Alamdari, S. Kaliaguine, Int. J. Chem. React. Eng. 4 (2006) A29.
[28] B. Levasseur, S. Kaliaguine, J. Solid State Chem. 181 (2008) 2953.
[29] J.M.D. Tascon, S. Mendioroz, L.G. Tejuca, Z. Phys. Chem. 124 (1981) 109.
[30] J.M.D. Tascon, S. Mendioroz, L.G. Tejuca, Z. Phys. Chem. 124 (1981) 249.
[31] S. Royer, A. Van Neste, R. Davidson, S. McIntyre, S. Kaliaguine, Ind. Eng. Chem. Res. 43 (2004) 5670.